Int. J. Therm. Sci. (2001) 40, 773–786

S1290-0729(01)01264-9/FLA

Detection of liquid mass fraction at the evaporator exit of refrigeration systems

Pega S. Hrnjak *, Mark A. Shannon, Todd M. Leicht, Norman R. Miller

Department of Mechanical and Industrial Engineering, University of Illinois at Urbana Champaign, 1206 W. Green, Urbana, IL 61801, USA

Abstract — The article presents four methods of detecting droplets in the stream of superheated vapor at the evaporator exit of refrigeration systems: (a) an energy balance, (b) a thin-film resistance (MEMS) sensor developed for this project, (c) a laser and photodiodes for measuring light scattered by entrained droplets, and (d) an exposed beaded thermocouple. Three configurations of the plate evaporator are examined, with refrigerant flow controlled by: (1) a thermostatic expansion valve, (2) a manual valve, and (3) a separate liquid injector used to examine the detection of controlled flow of droplets. The signals were recorded at both slow (0.5 Hz) and fast (40 Hz) rates in order to characterize the unsteady flow exiting the evaporator.

The presence of liquid in superheated vapor at the evaporator exit indicates nonequilibrium conditions and maldistribution of two-phase refrigerant within the evaporator. The performances of the MEMS sensor and the beaded thermocouple when exposed to small liquid mass fractions in a superheated vapor stream are examined to assess the feasibility of using each instrument to detect and control liquid mass fraction instead of superheat at evaporator exit and improve distribution among evaporator plates. Results show that the MEMS sensor is more sensitive to liquid mass fraction (LMF) in superheated vapor than the thermocouple at lower values. Both instruments in current versions exhibit a saturation point beyond which they can no longer detect increases in LMF. © 2001 Éditions scientifiques et médicales Elsevier SAS

superheat stability / plate evaporators / MEMS sensors / liquid mass fraction

Nomenclature

h_{eo}	refrigerant enthalpy at main evaporator exit	$kJ{\cdot}kg^{-1}$
h_{fg}	heat of fusion	$kJ{\cdot}kg^{-1}$
h_{mix}	enthalpy of refrigerant after the mixer	$kJ{\cdot}kg^{-1}$
h_{sat}	enthalpy of saturated vapor at exit pressure	$kJ{\cdot}kg^{-1}$
$\dot{m}_r$	refrigerant mass flow rate through main evaporator	$kg{\cdot}s^{-1}$
$\dot{m}_2$	refrigerant mass flow rate through secondary evaporator (bypass)	$kg{\cdot}s^{-1}$
T	period	s
$T_{e,glass}$	refrigerant temperature in glass tube at the evaporator exit measured by beaded thermocouple ($TC = T6 = T_{thermocouple} = T_{glassTC}$)	°C
T_{eo}	refrigerant exit temperature from the main evaporator (T_{rout})	°C
T_e	excess temperature above the saturation temperature of the boiling liquid	°C
T_{mix}	temperature at the static mixer exit	°C
T_{sat}	saturation temperature at evaporator exit	°C
T_{sensor}	temperature of the MEMS sensor	°C
$T_{s,1}$	temperature of the first resistor of the MEMS sensor	°C
$T_{s,2}$	temperature of the second resistor of the MEMS sensor	°C
$T_{s,3}$	temperature of the third resistor of the MEMS sensor	°C
T_{vapor}	temperature of the vapor only at the evaporator exit	°C
ΔT_{sup}	superheat at the evaporator exit	°C
P_{evap}	evaporating pressure	Pa
x_2	quality at the secondary evaporator exit	
α	temperature coefficient of the resistivity	$°C^{-1}$

INTRODUCTION: NONEQUILIBRIUM MIXTURE OF LIQUID DROPLETS IN SUPERHEATED VAPOR; LIQUID MASS FRACTION

Applications of parallel flow evaporators in refrigeration and air conditioning systems are increasing significantly due to their compactness and reduced refrigerant

* Correspondence and reprints.
E-mail address: pega@uiuc.edu (P.S. Hrnjak).

charge. These evaporators have multiple, typically vertical channels, mostly with plates or microchannel tubes. In direct expansion (DX) systems with controlled flow, refrigerant is expanded through a single throttling device such as a thermostatic valve (TXV) or some other type of expansion valve prior to entering the evaporator. Almost all flow control strategies use the superheat at the evaporator exit as the controlled variable.

Parallel flow evaporators suffer from refrigerant side maldistribution caused by either poor distribution at the inlet or uneven loads to each evaporator channel. This problem has been the object of numerous studies [3, 7–9]. In these evaporators the exit of one or several channels can be superheated while others have two-phase refrigerant at the exit. The result is a nonequilibrium mixture of droplets at the saturation temperature plus superheated vapor. An unsteady evaporator condition in horizontal round tubes was studied as early as the sixties [17] and continues to attract attention. More recent work by Peters and Barnhart [1] used P/DPA to investigate droplet distribution, velocity and size.

A number of patents have been filed in recent years [17, 18] for devices that aim to estimate the quality of liquid droplets in a refrigeration system. The devices appear to be aimed at permitting system application at much lower levels of superheat.

In this work we have are focused to the condition at the evaporator outlet where a liquid refrigerant and oil mixture is present as droplets and film in the stream of superheated vapor. Such nonequilibrium condition cannot be truly defined with the concept of vapor quality. For that reason we have defined the term liquid mass fraction (LMF) to mean the fraction of liquid refrigerant flow at any point in the total refrigerant flow stream which other part is superheated vapor.

After some time the droplets evaporate from the sensible heat of the vapor. As the temperature difference between the droplets at saturation temperature and the superheated vapor decreases, the state approaches equilibrium, and the LMF either becomes zero or $1 - x$ where x is quality.

Wedekind [16] has described the stochastic nature of the location of the last droplet in a uniformly heated and perfectly fed evaporator tube. This stochastic event can trigger hunting in evaporator-expansion valve control loop. This phenomenon is a limit cycle, which is commonly called “unstable” operation. Stability (amplitude and frequency of temperature, pressure, and mass flow fluctuations at the evaporator outlet) is of course, not only a function of the evaporator but also the feed back control design (TXV, EEV, etc.). Evaporator and valve interactions had been studied in [2, 3, 6, 19].

Our criterion for complete evaporation is a relatively steady temperature signal at the evaporator. When this occurs no refrigerant droplets are observed. Actually this is a very conservative approach. The refrigeration system can operate in a stable, non-hunting mode with some droplets exiting the evaporator.

Parallel flow evaporators typically require higher superheats than conventional evaporators with few circuits and large tube diameter as a consequence of imperfect distribution. The superheat needed to avoid unstable operation is often above 8 °C compared to 4–5 °C superheat for systems equipped with the conventional evaporators.

High superheat degrades evaporator performance as a consequence of lower heat transfer coefficients for superheated vapor versus those in the two-phase evaporating zone. Reducing superheat may cause liquid carryover that reduces the refrigeration effect where it is needed: in the evaporator. The opposite effects of increased heat transfer and lost refrigeration effect defines the exit condition that maximizes the coefficient of performance (COP) or capacity, assuming no undesired effects of valve hunting or excess compressor liquid return. Solberg et al., [14], have demonstrated the effect of exit conditions of automotive a/c systems with plate evaporators on capacity and COP. They use another version of the sensor described herein that has the same goal. They have shown that capacity and COP for the system are fairly flat with increasing LMF and that the maxima occur at different levels of LMF.

It appears that a sensor that does not use superheat at the exit as a control variable could be the basis for improved system operation. The sensor should detect a small liquid mass fraction in a superheated vapor stream and be incorporated into a feedback loop with the throttling device. A further improvement to DX systems using plate evaporators could be to incorporate these sensors with a multi-valve, active feedback flow control strategy where refrigerant expansion can be independently controlled in each channel or group of channels.

The objective of this article is to present successful ways of detecting LMF measuring the time-varying signals of several sensors at the exit of a plate evaporator. By correlating those variances with a time-averaged LMF in the superheated vapor stream we lay the groundwork for designing a control strategy that would increase evaporator performance. Controls developed using this approach with some modifications show very good results (see Solberg et al. [14]). In addition, by investigating the sensor

signals, it is possible to understand the nature of the non-equilibrium two-phase flow exiting the plate evaporator.

EXPERIMENTAL FACILITY

The system schematic is shown in *figure 1*. The facility can be conceptually divided into three main parts: the refrigeration loop, the water loop, and the evaporator exit test section. The refrigeration and the water loops provide conditions for the evaporator operation. Solid lines represent refrigerant piping, and dashed lines water piping. The working fluid is refrigerant R-22, with mineral oil added as a compressor lubricant. Subcooled refrigerant is expanded into the main evaporator and the bypass evaporator through two independent expansion devices. For certain tests, the combination of the main and secondary evaporators constitute a multi-channel evaporator in which maldistribution is manually induced. The bypass also provides a way to generate a known droplet flow. The main evaporator is a SWEP model B15X40 nominally 10 kW capacity plate heat exchanger, with upward flow of refrigerant. It is a very common evaporator design. It consists of 19 refrigerant channels and 20 water channels, with chevron style contours to enhance heat transfer. The heat load to the main evaporator was supplied by water from the water reservoir. Thermocouples located immediately at the inlet and the exit of the refrigerant and water streams monitor process conditions. Care was taken to position the exposed bead of the refrigerant exit thermocouple, T_{eo}, at the center of the exit pipe cross section. Depending on the experiments being performed, the main evaporator is fed by either a thermostatic expansion valve (TXV), or a manual valve (MXV). The bypass is always fed by a manual needle valve. The secondary evaporator is a 30 cm long 6 mm OD copper tube, and is used for certain experiments to inject up to 1.5 g·sec^{-1} of two-phase refrigerant into the inlet of the test section. The two-phase flow enters the test section as a uniform spray along the streamwise direction through several small holes drilled at the end of the 6 mm tube. The exit streams of both evaporators unite prior to the test section so that the combined flows could be measured.

The test section consists of a light scattering detection system, a MEMS thin-film resistance sensor, a thermocouple mounted in a glass tube, a static flow mixer, a heater, and several thermocouples and pressure transducers for monitoring flow conditions. The static flow

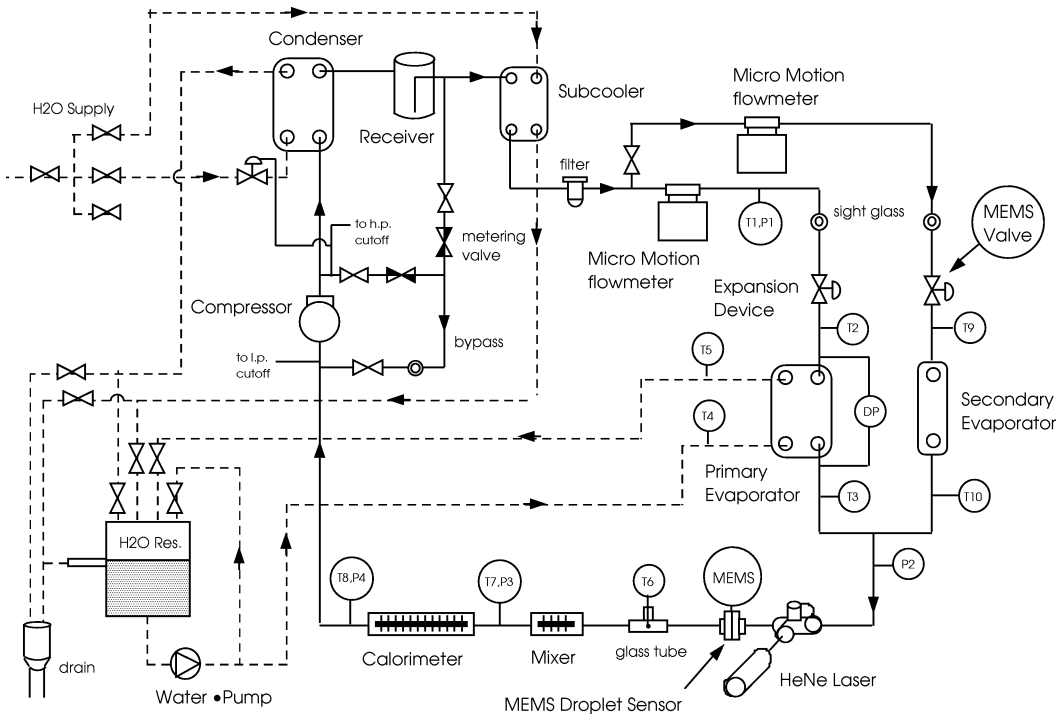

Figure 1. Flow schematic of the test facility.

mixer is a 15 cm long by 60 mm diameter copper tube with a helical copper sheet inside. It was designed to prolong the contact time so that refrigerant droplets entrained in the superheated vapor stream would be evaporated by the time they reach the exit of the mixer. Pressure drop across the mixer is marginal, and was never more than 3 kPa for all superheats and liquid mass fractions tested. The mixer is capable of evaporating up to 5% LMF at 10 °C superheat. The heater at the end of the test section is used as a precautionary measure to evaporate any remaining liquid when the condition at the mixer exit is saturated. The facility is equipped with *T* type (Cu–Co) thermocouples, two flowmeters, and several pressure transducers to monitor the system. Exposed beaded thermocouples are used, rather than the shielded type, because they provide a faster response time. Two mass flow sensors independently measure the refrigerant flow rates into the main and secondary evaporators. More details about the facility can be found in reference [12].

The evaporator exit flow entering the test section first encounters a light scattering detection system. *The light scattering detection system* consists of a 2 mW HeNe laser, a light chopper, two photodiodes, and two lock-in amplifiers. The laser beam is directed perpendicular to the flow direction, and a portion of the beam is scattered in all directions when entrained refrigerant droplets are present in the superheated vapor stream. Some of the scattered light is collected by a photodiode located 8 cm above the flow centerline. The unscattered portion of the laser beam is either absorbed by the refrigerant, or passed through to a second photodiode located across from the laser. The lock-in amplifiers are used to filter out unwanted frequencies, and noise, from the photodiode signals by referencing the laser beam chopper frequency. The magnitude of the lock-in output signal could then be correlated to the time-averaged LMF of the evaporator exit flow. The unfiltered signal from the scattered laser light photodiode is also used to detect the existence of entrained liquid and correlate the appearance of liquid with the MEMS sensor and thermocouple signals.

The thermocouple sensor is a type-*T* (Cu–Co) with exposed beaded junction. It is inserted into the glass tube of the test section. The glass tube is used for visual inspection and correlation to signal variances. The thermocouple sensor is fixed with a compression fitting using teflon ferrules so that the position of the bead could be adjusted within the tube cross section. The diameter of the thermocouple wire is 0.1 mm.

The MEMS sensor shown in *figure 2* consists of three separate serpentine nickel (Ni) resistors that are evaporated on a silicon wafer 400 μm thick. The serpentine

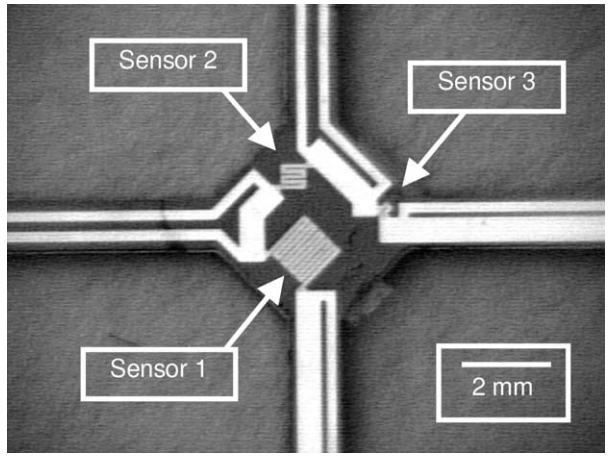

Figure 2. MEMS serpentine resistance sensors.

resistors, are ∼ 100 nm thick and measure 0.04 mm^2, 0.25 mm^2, and 1.0 mm^2 in total surface area. Three sensors on the same substrate allow for comparison the effect of sensor surface area on sensitivity to liquid droplets. A constant DC current, in the mA range, provides additional heating to evaporate droplets when striking the sensor. The evaporation of droplets on the sensor surface causes the sensor temperature and resistance to decrease. The thermal mass of the resistors is extremely small to give a very fast time response to refrigerant droplets impinging on the surface. The major thermal mass is the wafer.

At high superheats, or evenly distributed evaporator flows, the sensor works much like a hot wire anemometer, where the self-heating will cause the actual sensor temperature to be elevated above the free stream temperature. The extent to which the sensor temperature is higher will depend on the sensor current, the convective heat transfer coefficient between the sensor and the free stream, and the free stream temperature. Heat generated in the resistor, assisted with superheated vapor, can evaporate a number of droplets that strike the sensor. As increasing amounts of liquid strike the sensor, the sensor temperature is driven lower, until the sensor is completely saturated and can no longer evaporate droplets before the next one strikes. When the sensor is completely wetted, there is a thin film of boiling liquid covering the surface, so the sensor temperature will approach T_e, the excess temperature above the saturation temperature of the boiling liquid required to drive the boiling process. Thus, at any given time the sensor temperature can vary from an upper limit above the free stream vapor temperature to a lower limit

of T_e, which is slightly greater than T_{sat} determined at the evaporator exit pressure.

More details about the sensor and its response to refrigerant can be found in [12] and [13].

Global system parameters necessary for energy balance calculations were collected at 0.5 Hz (flow rates, pressures, temperatures, etc.) while test section instrumentation (the raw scattered light photodiode voltage, evaporator pressure, MEMS sensors, and all test section thermocouples) were sampled at 40 Hz. The sampling frequency, 40 Hz, was selected because it provided the best opportunity to capture all significant frequencies present in the thermocouple, MEMS sensor, and scattered light signals. During the shakedown process of the facility, Fourier analysis of the raw output of each instrument (thermocouple, sensor, scattered light) revealed that all frequencies above 10 Hz did not make a significant contribution to the power spectra. This Fourier analysis was performed on a 4-channel 1 GHz-sampling rate, digital oscilloscope. Therefore, the 40 Hz-sampling rate was selected as close as possible to the maximum expected frequency, while still being above twice the Nyquist frequency.

METHODS FOR CALCULATING LIQUID MASS FRACTION

Liquid mass fraction (LMF) is defined here as the ratio of mass flow rate of entrained liquid and the total mass flow rate where vapor is superheated, as opposed to quality where vapor is saturated:

$$\text{LMF}\,[\%] = \frac{\dot{m}_{\text{liquid}}}{\dot{m}_{\text{liquid}} + \dot{m}_{\text{vapor}}} \times 100 \qquad (1)$$

Two ways are used to determine LMF as indicated in *figure 4*: one with a static mixer when only the main evaporator is used, and the other when the bypass is used to generate a known LMF of measured flow. *The energy balance* (*or static mixer*) *method* is based on the reduction of vapor temperature at the static mixer due to the evaporation of droplets. *The direct method* determines the quality of the refrigerant flow immediately upstream of the instruments directly from flow rate, temperature and pressure measurements.

(a) Energy balance method. It is assumed that the droplets are completely evaporated and the vapor mixed before exiting the static mixer with no heat loss to the surroundings. State 2 (in *figure 3*) is at pressure P_{eo}. An

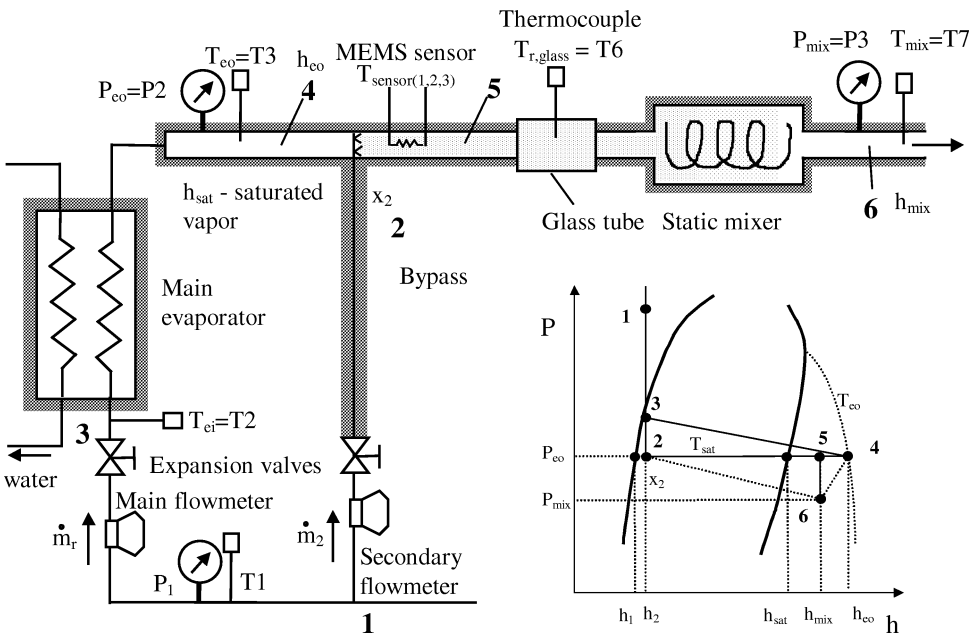

Figure 3. Determination of LMF at the evaporator exit when two phase mixture is injected in a superheated vapor stream at the evaporator exit.

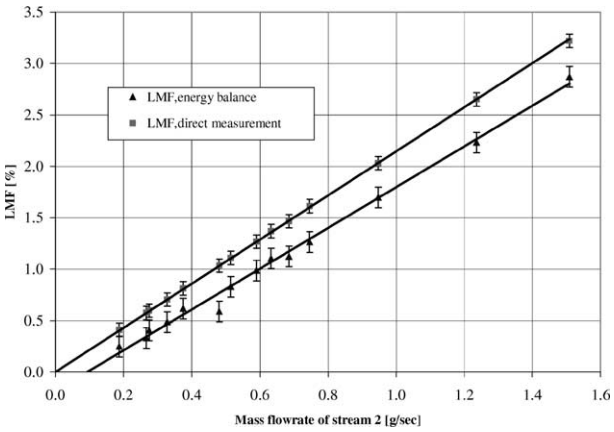

Figure 4. Comparison of LMF calculated from (a) static mixer energy balance method and (b) direct flow rate measurements.

energy balance of the adiabatic mixing of superheated vapor and a stream of known quality that comes out of the bypass evaporator (see *figure 3*) gives:

$$\dot{m}_{\mathrm{r}}(h_{\mathrm{eo}} - h_{\mathrm{mix}}) = \dot{m}_2(1 - x_2)h_{\mathrm{fg}} + \dot{m}_2(h_{\mathrm{mix}} - h_{\mathrm{sat}}) \quad (2)$$

The left hand side is the energy to cool the superheated vapor stream while the right hand side accounts for the energy gained by the low-quality mixture of stream 2. The first term is the heat of vaporization required to evaporate liquid droplets and the second term is the energy necessary to heat saturated vapor to the final state at the static mixer exit. The mass flow rates $\dot{m}_{\mathrm{r}}$ and $\dot{m}_2$ are measured, and all of the enthalpies can be determined from pressure and temperature measurements.

(b) Direct method. Stream 1 is superheated vapor exiting the main evaporator with a mass flow rate $\dot{m}_{\mathrm{r}}$, temperature $T_{\mathrm{eot}} = T3$ and pressure $P_{\mathrm{eo}} = P2$. For all test conditions the main evaporator runs with significant superheat ($> 8\,^{\circ}\mathrm{C}$), so it can be assumed with good accuracy that stream 1 is comprised solely of superheated vapor. Stream 2 is a lower quality mixture at pressure P_{eo} with mass flow rate $\dot{m}_2$.

The definition of LMF (3), can be modified to give the LMF directly from flow rates and stream 2 inlet quality:

$$\mathrm{LMF}\,[\%] = \frac{\dot{m}_2(1 - x_2)}{\dot{m}_{\mathrm{r}} + \dot{m}_2} \times 100 \quad (3)$$

The quality x_2 could be determined from the subcooled liquid temperature before expansion, $T1$ (state 1 in *figure 3*), and the pressure at the exit of the secondary evaporator, P_{eo}.

A comparison of both methods of calculating LMF for several experiments is shown in *figure 5*. Both sets of data show a linear relationship of LMF to m_2, the mass flow rate of stream 2. Error bars for each data point indicate only the instrument error associated with each measurement. Systematic error is evident—there is 0.2 to 0.4% offset. The true LMF at the inlet to the test section is most accurately represented by the direct measurement method (3). This statement is based not just on the fact that the direct method has less instrument error (smaller error bars), but because the static mixer energy balance method is based upon several simplifying assumptions. First, the energy balance method assumes no interaction between refrigerant and oil. The oil present in the suction line (measured to be 0.2 to 0.3%) will absorb liquid droplets, thereby preventing them from evaporating. This causes a negative departure of the calculated LMF from the true LMF. Second, the energy balance method assumes complete evaporation (no droplets left) and mixing of the two streams before the static mixer exit. Third, it assumes that the walls of the mixer are adiabatic.

CONDITIONS AT THE EVAPORATOR EXIT

Characterization of the signal at the evaporator exit at superheat 8–10 °C is presented in *figures 5–7*. Refrigerant and water inlet temperatures to the evaporator are kept as close as possible to 2 °C and 12 °C, respectively, which is typical for a/c water chillers. Each figure has three cases:

(1) thermostatic expansion valve (TXV) control,
(2) manual expansion valve (MXV) control, and
(3) controlled LMF. The secondary evaporator (bypass) is not used in the first two cases. Each case has three graphs:
(a) slow (0.5 Hz), and
(b) fast (40 Hz) sampling rates, both in time domain, and
(c) in frequency domain.

The difference between case (1) and (2) show the effect of the TXV on the exit signal and will be discussed later. Case (3) shows the condition when a secondary, bypass evaporator supplies droplets at measured rate to the superheated vapor at the main evaporator exit.

Each graph in the time domain has four readings. At low sampling rates in (a) there are no MEMS sensor readings. The beaded thermocouple T_{vapor} is positioned such that it is protected against droplet strikes. The thermocouple $T_{\mathrm{e,out}} = T_{\mathrm{eo}}$ is affected by droplets in the suction line. T_{sat} is the temperature determined by

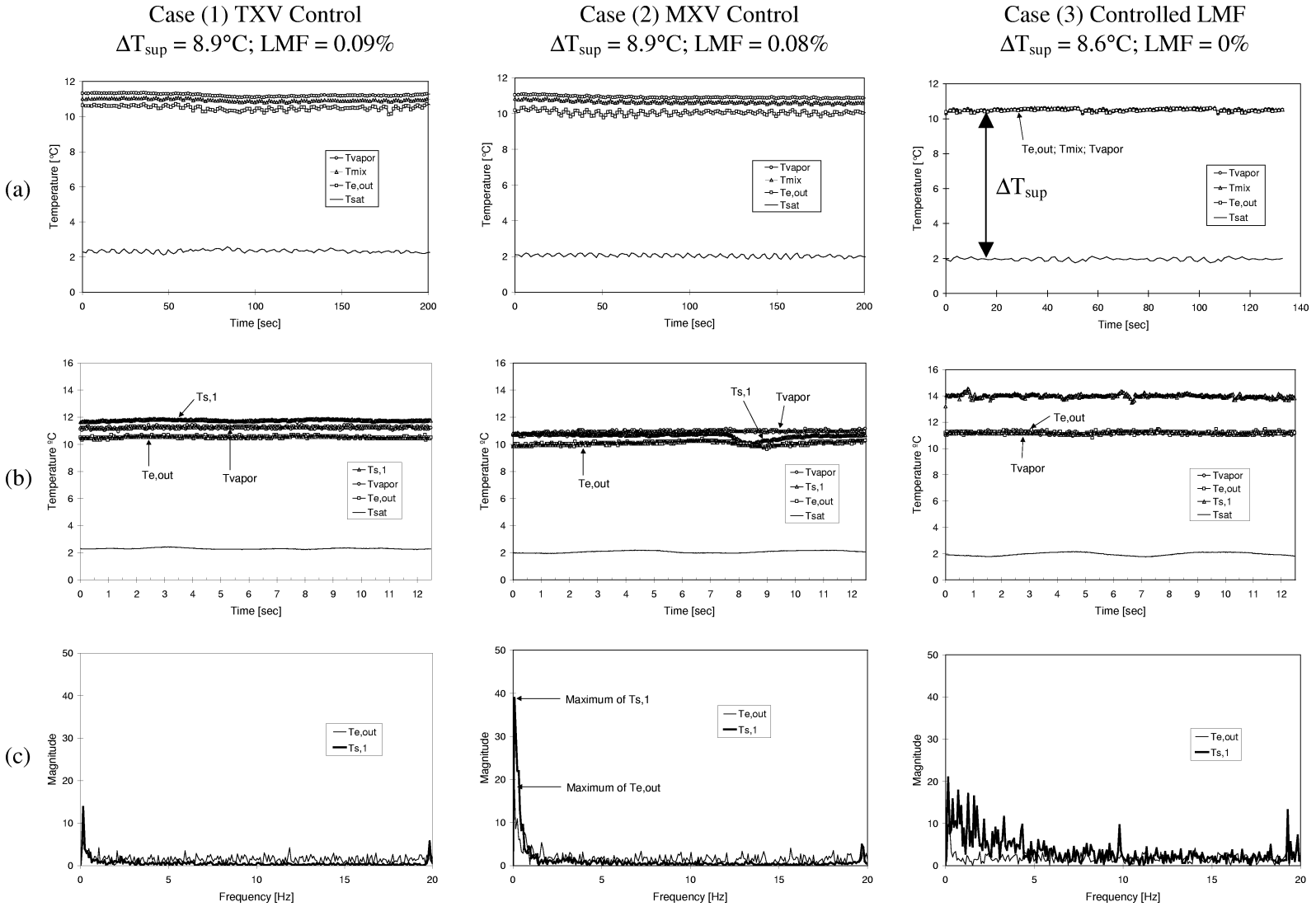

Figure 5. Evaporator outlet temperature signal comparison at low LMF during TXV control, MXV control, and simulated maldistribution. For simulated maldistribution evaporator outlet was manually controlled for high superheat and two phase was injected downstream using a bypass: (a) During the entire run at 0.5 Hz sampling rate; (b) At 40 Hz sampling rate; (c) In the frequency domain.

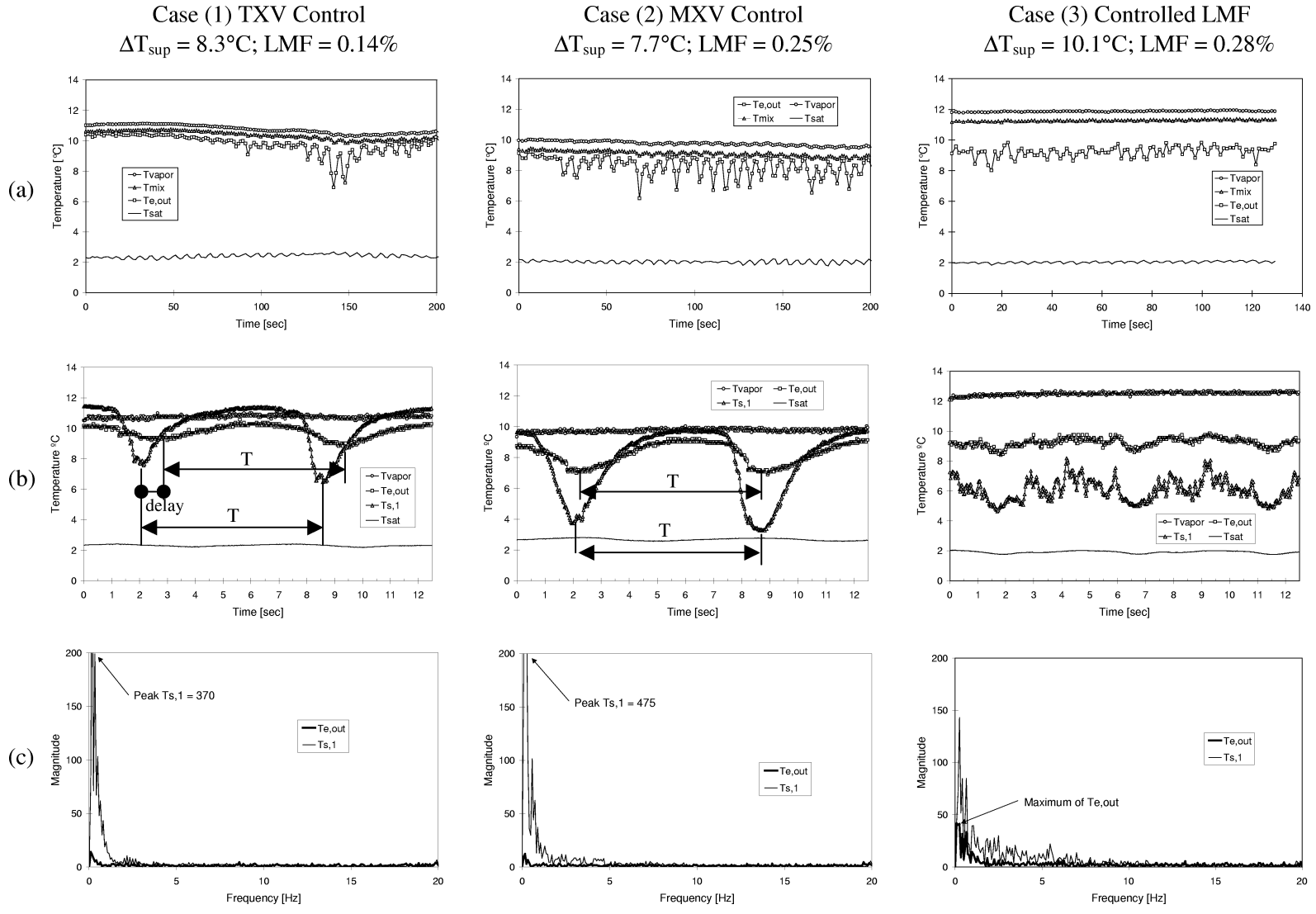

Figure 6. Evaporator outlet temperature signal comparison at medium LMF during TXV control, MXV control, and simulated maldistribution. For simulated maldistribution evaporator outlet was manually controlled for high superheat and two phase was injected downstream using a bypass: (a) During the entire run at 0.5 Hz sampling rate; (b) At 40 Hz sampling rate; (c) In the frequency domain.

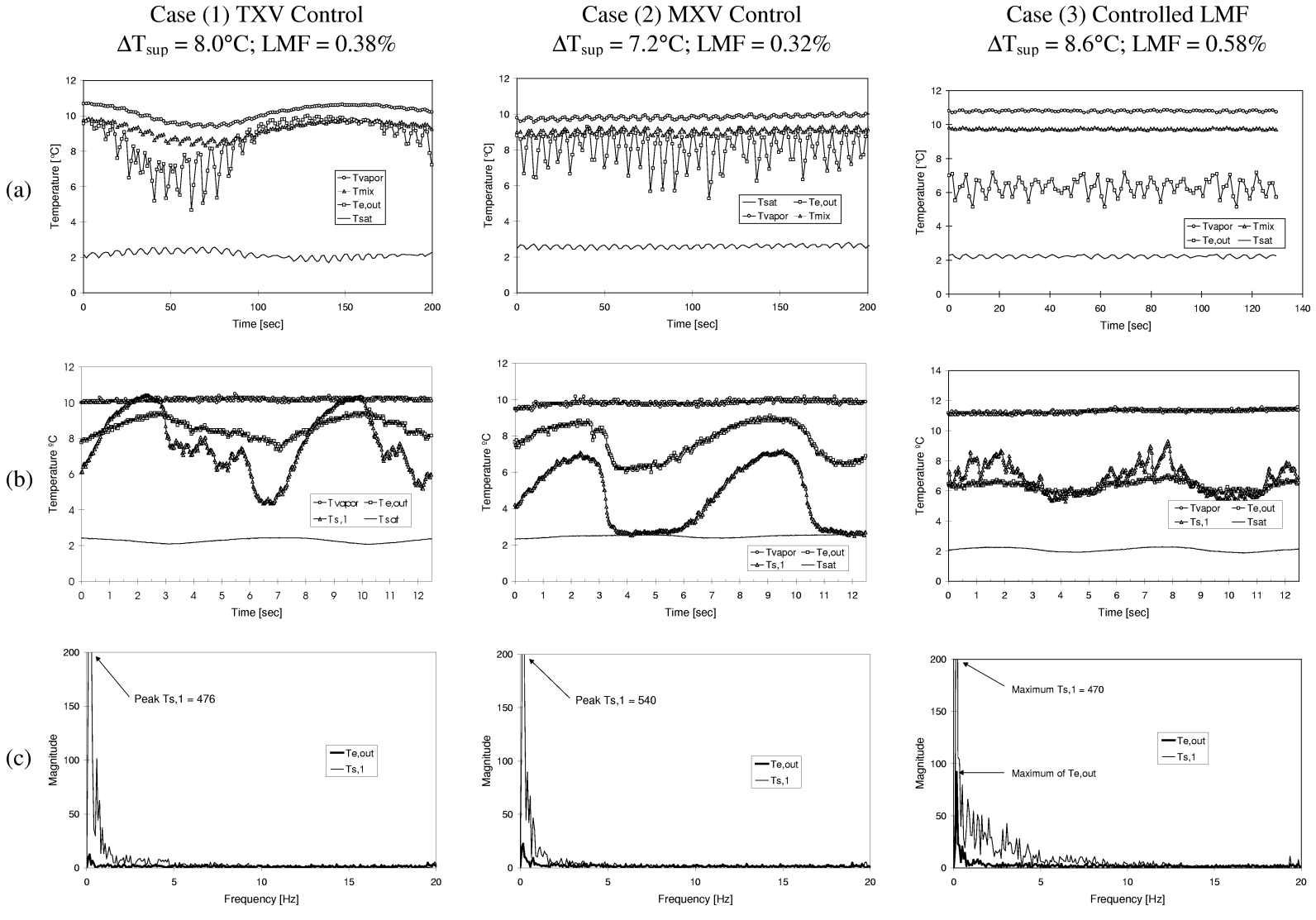

Figure 7. Evaporator outlet temperature signal comparison at high LMF during TXV control, MXV control, and simulated maldistribution. For simulated maldistribution evaporator outlet was manually controlled for high superheat and two phase was injected downstream using a bypass: (a) During the entire run at 0.5 Hz sampling rate; (b) At 40 Hz sampling rate; (c) In the frequency domain.

pressure at the evaporator exit. T_{mix} is the temperature after the static mixer. Superheat ΔT_{sup} is indicated in the diagram by arrows. In row (b) the temperature reading of $T_{s,1}$ of the MEMS sensor replaces T_{mix}. The scale for the temperature in row (b) is changed to accommodate the higher reading of the $T_{s,1}$. At low LMF, heating by the MEMS sensor is greater than the convective cooling in superheated vapor, and thus the temperature reading increases beyond T_{vapor}.

Figure 5 shows conditions at the evaporator exit that can be classified as superheated vapor, with a very low or zero LMF. The temperature at the exit of the static mixer, T_{mix}, and the evaporator exit T_{eo} in all runs shown in *figure 5* are almost equal, indicating that no liquid evaporates in the static mixer (assuming an adiabatic mixing). The static mixer extends the time for the liquid-vapor interaction to occur, causing the droplets (if any) to evaporate before the mixer exit. The reading of T_{vapor} is a very important baseline for the case when the thermocouple at the evaporator outlet $T_{eo} = T_{e,out}$ is impacted by refrigerant droplets. The small difference between T_{vapor} and $T_{e,out}$ in *figure 5* can be attributed to the effect of minor LMF and a very small heat exchange with the environment.

In *figure 6*, results of three runs in which the LMF was significantly greater than zero are shown. Note that in case (1), T_{vapor} appears to be constant at 11.8 °C for the entire run, but T_{mix} is as much as 1 °C lower. This small temperature difference amounts to 0.2 g·s^{-1} of liquid out of the total 52 g·s^{-1} flowing through the evaporator, calculated by the energy balance method. Thermocouple readings of $T_{e,out}$ at low sampling frequency in row (a) indicate the presence of liquid by the reduction in $T_{e,out}$ and its oscillatory behavior. Periodic temperature change is even more obvious in the graphs with higher (40 Hz) sampling rate in row (b). T_{eo} cyclically deviates from T_{vapor} approximately every 7 s. It was also visually observed in those time intervals that clouds of droplets pass through the glass tube. There is almost no difference between cases (1) and (2) in row (b). In each case, the MEMS sensor is more affected by liquid than the thermocouple, as seen by the greater amplitude of the fluctuations. The periods T are the same, but the thermocouple reading has a phase shift as a consequence of a greater thermal mass of the thermocouple junction. The slightly smaller amplitude in case (1) than in case (2) is a consequence of a slightly lower LMF (0.14% (1) vs. 0.25 (2)). Notice that the oscillation period T is identical when the TXV is used (case (2)) and when the expansion valve was set manually (case (2)). The time varying signal is not the consequence of the TXV operation, but the evaporator dynamics. Due to different thermal load, pressure drop, flow pattern, and distribution in inlet header flow pulsation expulse some two-phase fluid to the exit. This phenomenon is described by Wedekind [16] and Barnhard and Peters [1].

A comparison with case (3) supports the evaporator dynamic hypothesis. In case (3), the low LMF condition is generated by mixing stable superheated vapor at the evaporator exit with wet vapor injected from the secondary bypass evaporator. Unsteady, pulsating flow of two-phase refrigerant from the main evaporator does not occur because the superheat is sufficiently high to evaporate all droplets within the evaporator plates.

The $T_{s,1}$ signal in case (3) row (b) indicates higher frequency content than thermocouple $T_{e,out}$. This is because the MEMS sensor has a smaller thermal mass, and can sense droplet impingement. The thermocouple signal essentially follows the dynamics of $T_{s,1}$ but acts as a low pass filter or averager, removing the high frequency fluctuations.

Rows (a) and (b) in *figure 7* show the unsteady temperature at the evaporator exit at increasing LMF. As liquid exits the evaporator creating higher LMF, the thermocouple $T_{e,out}$ reading will drop significantly below T_{vapor} due to the cooling effect of the droplets. The effect of unsteady cycling that can be attributed to the TXV feed back control can be seen in row (a) through a long periodicity of exit temperature (approximately 180 s). This behavior of $T_{e,out}$ is an indication that unstable superheat control for the system has been approached. The periodic dips (every 7 s), which are clearly recognizable at the 40 Hz sample frequency in row (b), are a consequence of the unsteady process in the evaporator. Notice that the same $T = 7$ second period can be seen in case (2)(b) and in *figure 6*.

In case (3), cyclic operation does not occur. This is because the exit of the main evaporator is always superheated. The unsteady location of the end of the two-phase zone is deep inside the evaporator plates. As a result, no droplets are expelled at the evaporator exit.

The time trace of T_{s1} in *figure 7* dips drastically downward toward the saturation temperature and stays there even longer than in *figure 6*. These temperature depressions are visually correlated to puffs, or clouds of droplets in the evaporator exit pipe. The exit thermocouple temperature is bounded by the warm superheated vapor temperature on the high side, and the saturation temperature on the low side.

Greater variance and higher frequency content of the MEMS sensor signal in case (3) indicate earlier detection of smaller droplets (see *figures 5–7*). A heated sensor of

small thermal mass can evaporate droplets more quickly, and provide fast response to rapidly changing evaporator exit flow conditions. Nevertheless, the MEMS sensor is less capable of detecting denser clouds of droplets that are the consequence of evaporator dynamics, rather than entrained liquid.

Additional information about the exit signal as well as performance of the thermocouple and MEMS sensor can be obtained by examining the frequency content of the signals. The power spectra are shown in row (c) in *figures 5–7*. Fast Fourier Transform analysis was performed on the discrete temperature signals using HP-VEE™ software, by first subtracting the mean of each signal from the original data set. This was done to remove the DC component of the each signal, thereby leaving only the oscillating portion of the temperature caused by both impingement of liquid droplets and saturation temperature fluctuation. The first large spike at 0.16 Hz is due to the saturation temperature fluctuation. All of the other frequencies can be attributed to the presence of liquid droplets. The significant frequencies die out around 5 Hz. Initially, it was thought that the MEMS sensor would be able to detect individual droplet impacts at frequencies above 100 Hz. This is clearly not the case, especially at the higher LMF's when droplet clouds containing thousands of large droplets are observed visually in the glass tube. However, at low LMF's (less than 0.7%) where the sensor is most sensitive, droplet clouds were not seen by the naked eye.

NON-EQUILIBRIUM CONDITIONS AT THE EVAPORATOR EXIT MEASURED BY DIFFERENT INSTRUMENTS

Table I presents the results of 19 separate runs conducted over 3 different superheats (11.6 °C, 10.0 °C, and 8.5 °C), and a LMF from 0 to 2.5% with the nominal mass flow rate of 40 g·s^{-1}. The LMF is controlled in each case by the secondary bypass evaporator. Two sets of graphs given in *figures 8–10*, and *figures 12* and 13 shed more light on these issues.

Figures 8–10 have three lines that show three temperature differences: (i) the superheat ($\Delta T_{sup} = T_{rout} - T_{sat} = T_{eo} - T_{sat}$), (ii) the temperature difference between the thermocouple located in the glass tube affected by droplets and saturation temperature ($T_{eo} - T_{sat}$), and (iii) the temperature difference between the MEMS sensor temperature and saturation temperature ($T_{sensor} - T_{sat}$), all as a function of LMF for a given superheat. In these runs $T_{eo} = T_{rout}$ is approximately same as T_{vapor} shown

TABLE I
Summary of conditions for simulated maldistribution runs. Complete time histories of these temperature for each run can be found in Shannon, Hrnjak and Leicht, 1998.

Run	LMF [%]	ΔT_{sup} [°C]	T_{eo} [°C]	T_{mix} [°C]	P_{evap} [kPa]	Sensor current [mA]
1	0	11.6	13.5	13.6	529.8	24.64
2	0.41	11.9	14.0	13.2	531.8	24.98
3	0.60	11.8	13.9	12.7	532.2	24.98
4	0.81	11.7	13.8	11.9	531.8	24.94
5	1.11	11.5	13.8	11.2	535.4	25.01
6	1.37	11.6	13.8	10.5	533.9	24.96
7	1.61	11.7	13.8	10.0	533.6	25.40
8	2.65	11.3	13.7	7.1	538.6	25.37
9	0	10.4	12.4	N/A	530.1	24.95
10	0.32	10.0	12.1	11.4	532.6	25.00
11	0.61	9.9	12.2	10.7	534.3	24.56
12	1.28	9.7	12.1	9.3	537.8	24.56
13	0	8.6	10.5	10.5	528.4	25.04
14	0.58	8.6	10.8	9.7	533.7	25.00
15	0.71	8.6	10.8	9.2	533.2	25.00
16	1.04	8.3	10.7	8.8	536.2	25.44
17	1.27	8.2	10.5	7.6	535.6	24.62
18	1.47	8.4	10.6	7.3	534.6	25.13
19	2.03	8.4	10.7	5.7	536.5	25.11

in *figures 5–7*. The bars on the thermocouple and sensor temperature points in *figures 9–11* indicate the range of temperatures measured during the entire 12.5 s of data collection time, e.g., variance of the thermocouple. The bars show the sensitivity of the thermocouple and MEMS sensor to the presence of liquid. Those bars are calculated based on readings shown in time domain diagrams like in *figures 11* and *12*. In all three figures, the MEMS sensor is much more sensitive at lower LMF's. The thermocouple, however, is more sensitive at higher LMF, mostly around 1.5%. As the LMF increases, the droplets eventually saturate the readings and both the mean temperature and the variance reach a steady value. Average readings of both thermometers are proportional to LMF. Saturation temperature, or zero superheat, is the expected asymptotic value reached by the thermocouple. The MEMS sensor reaches a temperature associated with the excess temperature T_e above T_{sat}, see reference [13].

Figures 11 and *12* show the temperature of the beaded thermocouple located in the glass tube $T_{glassTC}$, MEMS sensor temperature (for the largest sensor, R1), saturation temperature T_{sat} based on the pressure reading, and scattered laser light photodiode voltage in the time domain for low (*figure 11*), and high (*figure 12*) liquid mass fractions. *Figure 11* graphically shows a small variance in the thermocouple reading $T_{e,glass}$ and a high

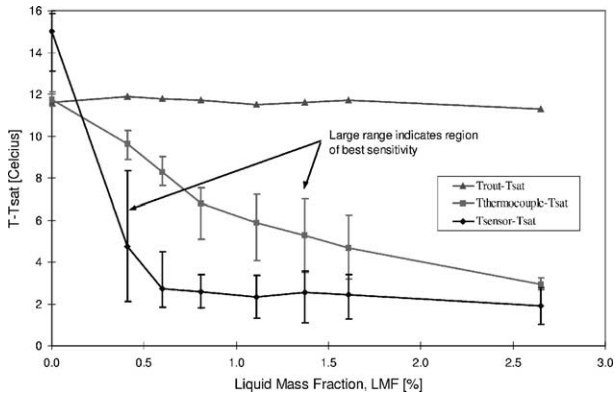

Figure 8. Summary of runs 1–8 with nominal superheat $\Delta T_{\text{sup}} = 11.6\,^{\circ}\text{C}$. Bars indicate variance of temperatures measured, i.e., fluctuations due to droplet impacts.

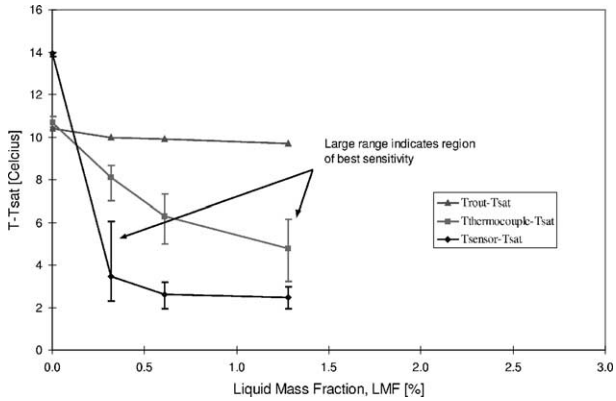

Figure 9. Summary of runs 9–12 with nominal superheat $\Delta T_{\text{sup}} = 10\,^{\circ}\text{C}$.

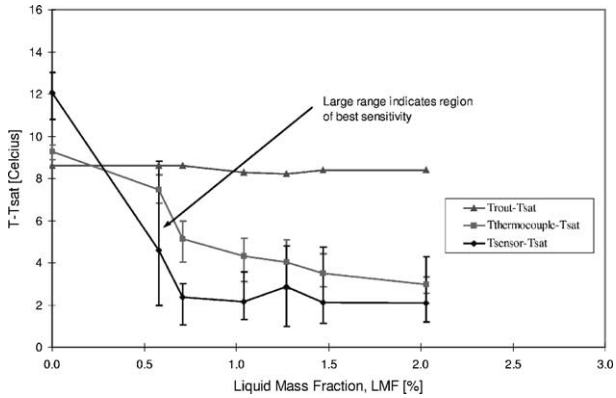

Figure 10. Summary of runs 13–19 with nominal superheat $\Delta T_{\text{sup}} = 8.5\,^{\circ}\text{C}$.

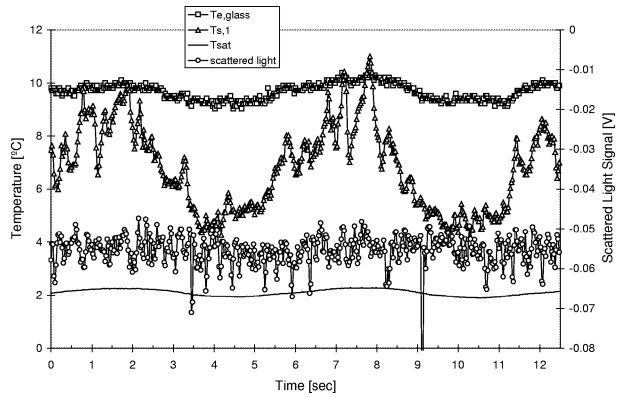

Figure 11. Thermocouple, MEMS sensor, and scattered light signals in the time domain at low LMF. (Data shown for run 14; LMF $= 0.58\%$; superheat $\Delta T_{\text{sup}} = 8.6\,^{\circ}\text{C}$).

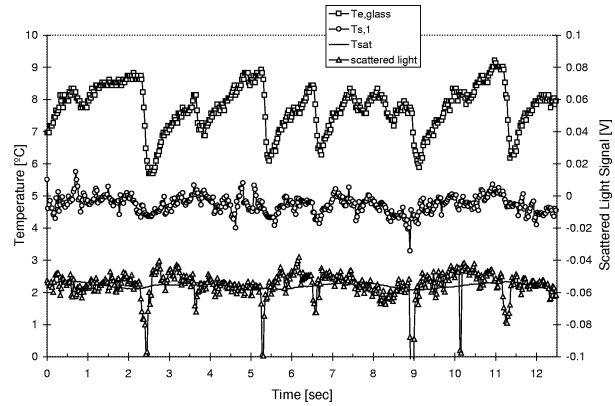

Figure 12. Thermocouple, MEMS sensor, and scattered light signals in the time domain at high LMF (data shown for run 6; LMF $= 1.37\%$; superheat $\Delta T_{\text{sup}} = 11.6\,^{\circ}\text{C}$).

variance in the MEMS sensor $T_{\text{s},1}$, for a low LMF (0.58%) and superheat of 8.5 °C. Contrast those results with *figure 12*. Exactly the opposite is true at a high LMF (1.37%) and higher superheat (11.6 °C). The results show that the MEMS sensor is most sensitive to the presence of droplets at low LMF. This is shown by the large amplitude temperature fluctuations of the sensor, compared to relatively small temperature fluctuation by the thermocouple. In *figure 12*, where LMF is high (LMF = 1.37%) the MEMS sensor is unable to detect the increasing amount of liquid due to saturation, but the thermocouple now is becoming more sensitive to liquid. At the higher LMF, the temperature fluctuations of the thermocouple are larger, and those of the MEMS sensor are decreased.

There are both slow and fast frequency components in the thermocouple and the MEMS sensor temperature

traces. The slow frequency component in both temperatures is exactly in phase with the saturation temperature displayed on the bottom of the figures. Saturation temperature varies with evaporation temperature, which oscillates due to the nature of the two-phase evaporating flow in the evaporator. Superimposed on top of the slow fluctuation is the high frequency content. The high frequencies are a result of droplets impinging on the surface of the MEMS sensor and thermocouple.

The trace of the scattered laser light photodiode voltage in both figures gives a relative indication of the amount of liquid present during the run. In *figure 11*, when the LMF is only 0.58%, the scattered light signal amplitude fluctuation is about 0.01 V, but in *figure 12*, when LMF = 1.37%, the amplitude variation is higher. There are also several large amplitude spikes on the order of 0.5 V. These larger spikes are related to large clouds of droplets that were visually observed through the glass tube mounted in the test section. Notice that during relatively high LMF (*figure 12*) the thermocouple temperature $T_{e,glass}$ drops rapidly after the passage of a droplet cloud, but the MEMS sensor is unable to respond to the additional liquid, again showing the saturation of the sensor. This phenomenon is fully discussed in [13].

SUMMARY AND CONCLUSIONS

Non-equilibrium flow of dispersed droplets at the saturation temperature in a superheated vapor at the outlet of a plate evaporator fed by a TXV and MXV was studied over a range of superheats from 12 °C to 7 °C. The liquid droplets come in discrete mists, or clouds, at regular intervals, as a consequence of evaporator dynamics. Reducing superheat below 8 °C caused the thermostatic expansion valve to hunt. At the onset of hunting operation with the TXV used, the time-averaged LMF of entrained refrigerant droplets was measured to be 0.4%. Droplet mist generation still occurred every 7 s during TXV hunting, but the characteristic saw tooth temperature signal was superimposed over a slower mean temperature fluctuation with a period of nearly 3 min.

The presence of these droplet mists was detected visually through the glass tube in the test section, but also by a MEMS sensor, a thermocouple, and confirmed by measurements of scattered laser light intensity. MEMS thin-film resistance sensors with three resistors were designed, fabricated, and calibrated against known liquid mass fractions for the purposes of this investigation. The three resistors varied in size, but all had the same surface heat flux. They are driven with a small constant DC current (25 mA) to provide self-heating to boil liquid droplets that strike the sensor.

Performance of the MEMS sensor was investigated over a range of liquid mass fraction up to 4%, and superheat temperatures from 8 °C to 12 °C. Data collected over these conditions indicates that the sensor is best used when liquid fractions are below 1%. Greater amounts of liquid tend to saturate the sensor, and prevent it from boiling off the excess liquid. The ability of the MEMS sensor to detect a small entrained LMF was compared to that of an exposed beaded thermocouple, with encouraging results. Although the thermocouple can indicate the presence of droplets over a wider range of LMF, the heated MEMS sensor has a much greater sensitivity than the thermocouple for low LMF.

Results show that the prototype MEMS thin-film resistance sensor can detect liquid droplets and the mists entrained in the superheated vapor exiting plate evaporators. Variance of the measured temperatures could be used as a control signal with calibration as shown in *figures 8–10*.

By correlating those variances with a time-averaged LMF in the superheated vapor stream the groundwork for designing a control strategy that would increase evaporator performance is laid out. In addition, by investigating the sensor signals, it is possible to understand the nature of the non-equilibrium two-phase flow exiting the plate evaporator.

Further development of sensors is underway with the objective of improving robustness, increasing the range of operating parameters and developing actuation and control strategies for system operation.

Solberg et al., [14] quantify the effect of the control strategy with the new sensor to system capacity and coefficient of performance.

Acknowledgements

The authors gratefully acknowledge support from the Electric Power Research Institute (EPRI), contract #8511-08, and Air Conditioning and Refrigeration Center (ACRC), of the University of Illinois at Urbana-Champaign.

REFERENCES

[1] Barnhart J.S., Peters J.E., An experimental investigation of flow patterns and liquid entrainment in a horizontal-tube evaporator, ACRC TR-28, Air Conditioning and Refrigeration Center, University of Illinois at Urbana-Champaign (1992).

[2] Broersen P.M.T., van der Jagt M.F.G., Hunting of evaporators controlled by a thermostatic expansion valve, J. Dynamic Syst. Measurement Control 102 (1980) 130–135.

[3] Das Sarit K., Spang B., Roetzel W., Dynamic behavior of plate heat exchangers—experiments and modeling, J. Heat Transfer 117 (1995) 859–864.

[4] Dowling M.F., Wartell J.D., Jeter S.M., Moisture fraction measurements for two-phase mist flow using high-sensitivity capacitance sensors, Nuclear Technology 117 (1997) 353–365.

[5] Farrar B., Samways A.L., Ali J., A computer-based hot-film technique for two-phase flow measurements, Measurement Sci. Technology 6 (1995) 1528–1537.

[6] Gruhle W.-D., Isermann R., Modeling and control of a refrigerant evaporator, J. Dynamic Syst. Measurement Control 107 (1985) 235–240.

[7] Hewitt N.J., McMullen J.T., Moran D.G., The control of a refrigeration system using a compact plate heat exchanger as an evaporator, Internat. J. Energy Res. 17 (1993) 393–399.

[8] Khan A.R., Baker N.S., Wardle A.P., The dynamic characteristics of a countercurrent plate heat exchanger, Internat. J. Heat Mass Transfer 31 (6) (1988) 1269–1278.

[9] Lakshmanan C.C., Potter O.E., Dynamic simulation of plate heat exchangers, Internat. J. Heat Mass Transfer 33 (5) (1990) 995–1002.

[10] Lee S.L., Yang Z.H., Hsyua Y., Cooling of a heated surface by mist flow, J. Heat Transfer 116 (1994) 167–172.

[11] Outtagarts A., Haberschill P., Lallemand M., The transient response of an evaporator fed through an electronic expansion valve, Internat. J. Energy Res. 21 (1997) 793–807.

[12] Shannon M.A., Hrnjak P.S., Leicht T.L., Exploratory research on MEMS technology for air-conditioning and heat pumps, EPRI report TR-111699, 1998.

[13] Shannon M.A., Leicht T.L., Hrnjak P.S., Miller N.R., Kahn F.A., Thin-film resistance sensor for measuring liquid mass fraction on super-heated refrigerant, Sensors and Actuators (2000), to appear.

[14] Solberg J.R., Miller N.R., Hrnjak P.S., A sensor for estimating the liquid mass fraction of the refrigerant exiting an evaporator, SAE paper 2000-01-0976 (2000).

[15] Stoecker W.F., Stability of an evaporator-expansion valve control loop, ASHRAE Trans. 72 (1966), part 2.

[16] Wedekind G.L., Transient response of the mixture-vapor transition point in two-phase horizontal evaporating flow, Ph.D. thesis, University of Illinois at Urbana-Champaign, 1965.

[17] Cornwall K., UK Patent 2219661B, 1992.

[18] US Patents: #5289692, 1994, #5335513, 1994, #5390897, 1995, #5460349, 1995, #5477701, 1995, #5522231, 1996.

[19] Lenger M., Hrnjak P.S., Jacobi A.M., Superheat stability of an evaporator and thermostatic expansion valve, ACRC report TR-138, Urbana, IL, 1998.